Multi-functional thermal-mechanical anisotropic metasurface with shape memory alloy actuators

Chhunheng Lor, Ratanak Phon, Minjae Lee, Sungjoon Lim *

School of Electrical and Electronic Engineering, Chung-Ang University, Heukseok-Dong, Dongjak-Gu, Seoul 06974, Republic of Korea

HIGHLIGHTS

- Composes by two groundless metasurfaces.
- Switchable between 96.5% absorptivity and 81.33% reflectivity at 10.5 GHz.
- Transmission enhancement ratio of 11.02 dB for opposite direction EM wave at 5.9 GHz.
- Side thermal compression shape memory alloy spring as moving mechanism.

GRAPHICAL ABSTRACT
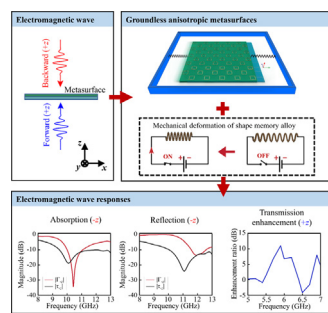
ABSTRACT

Metasurfaces are two-dimensional (2D) artificial electromagnetic (EM) materials comprising subwavelength periodic or non-periodic arrays of resonator elements. Multi-functional metasurfaces have shown magnificent potentials for many applications, including wireless communication, radar systems, and security. EM functions of metasurfaces can generally be switched or controlled by electrical or optical components, but these conventional tuning technologies suffer from complexity, high cost, and design limitations for large scales and function integration. Therefore, this paper proposes a novel thermal–mechanical anisotropic metasurface to provide multiple functionalities through mechanical transformation due to thermal stimulus on two shape memory alloy actuators, switching EM functionality between absorption and reflection. The absorptivity and reflectivity at 10.5 GHz are 96.5% and 81.33%, respectively. It consists of the motional metasurface and stational metasurface where mechanical transformation is achieved by the motional metasurface. In addition to the mechanical transformation, its function is switched depending on incident EM wave direction due to anisotropy that could achieved the transmission enhancement in ratio of 11.02 dB at operation frequency 5.9 GHz in opposing excitation. The proposed idea is numerically and experimentally demonstrated and discussed.

1. Introduction

Metamaterials are artificial composite structures with electromagnetic (EM) properties derived from the arrangements of the subwavelength building block of the array of resonator elements rather than the compositions of the natural materials [1–3]. Metamaterials have attracted strong research and industrial attention due to their unique EM properties and can be constructed using various types materials to achieve multiple properties and functionalities. Consequently, many metamaterials, metadevices, and metasurfaces have been explored, including invisible cloaks [4–6]. super lenses [7,8], polarization converters [9,10], radar cross section (RCS) reduction [11–13], holography [14,15], beam

deflection [16,17], and analog computation [18,19]. As a counterpart of three-dimensional (3D) metamaterials, Metasurfaces are two-dimensional (2D) planar has overcame with several challenges of its construction to reduce complication, bulky, lossy, large-scale manufacturing, and integration with other devices.

Tunable or reconfigurable metasurfaces have received strong research attention due to their multi-functionality compared with passive structures [20–26]. Several research groups have proposed techniques and methodologies to create tunable or EM functions switching metasurfaces. Active metasurfaces, i.e., their EM functionalities can be electrically controlled by external stimuli, are mainly used for high-speed applications, where they are commonly integrated with active electrical components including transistors, varactors, and PIN diodes, to create self-switchable, programmable, and/or self-adaptive reprogrammable metasurfaces, i.e., smart or intelligent metasurfaces [27–32]. However, smart metasurfaces require considerable an enormous among of active components, which are required DC power consumption and biasing network, and other controlling systems, including sensors and microcontroller units, to sense and adjust their working functionality. On the other hand, several advanced material technologies have been shown its potential in speedy switch and high ratio tune EM function, e.g. vanadium dioxide (VO_2), liquid crystal, and graphene [33,34]. However, these technologies still remain costly and require basing network [35].

Mechanical devices have been widely studied recently to reduce complexity and achieve simple tuning or switching mechanisms [36–39]. For example, origami based metal walls with mechanically controlled EM absorption magnitude and deflection angle have been proposed [40], using shape memory polymer (SMP) smart material as a simple tuning mechanism; a spatial modulation metasurface was recently proposed to simultaneously realize beam splitting and steering between left and right-hand circularly polarized waves [41]; and 2D electromechanically transformable metasurfaces with beam steering capability have been realized by controlling shape memory alloys (SMAs) [42]. Although several simple and low-cost mechanical metasurfaces have been proposed, mechanical metasurfaces with different integrated functionalities, RCS reduction, reflection, transmission, EM wave enhancement, etc. have not been explored and remain challenging to design. In addition, although many multifunctional metasurfaces based on incident direction of EM wave has been reported, their metasurface are polarization dependance [43], passive metasurface [44], and has function limitation with using single layer structure [45].

This work proposes a reconfigurable anisotropic metasurface with multi-functional characteristics. The proposed metasurface comprises two sub-metasurfaces that can move independently, by incorporating with two SMA actuators to move one of those sub-metasurfaces for generating different patterns, specifically, with different output impedances. Since effective impedance depends on metasurface movement, the proposed metasurface can realize reconfigurable functionalities between absorption and reflection functions. Although we use two spring pitches for controlling the transformation, the proposed metasurface retains the incident wavefront insensitive polarization properties, and we can realize EM wave enhancement for the opposite excitation with its anisotropic design. Experimental results confirm good agreement with numerical simulations. We believe the proposed concept will be useful for future mechanical based multi-functional EM devices.

2. Theoretical design

2.1. Conception and design

Metasurface absorbers are commonly used in stealth technology or electromagnetic wave protection applications, helping to prevent radar detection by reducing radar emission. Most conventional designs use a full metallic ground plane to prevent transmission entirely and minimize reflection by optimizing the top patterns to match the free space impedance and enhancing absorptivity. However, that conventional multi-functional metasurface designs are limited for absorption integrated function, e.g., incident EM wave from the opposite direction is generally reflected due to the complete metallic ground. This study designed a thermal–mechanical anisotropic metasurface (TMAM) to provide multiple EM functionalities for both incident wave directions. As shown in Fig. 1, the mechanical reconfigurable metasurface consists of two layers: the motional and stational metasurfaces on the upper and lower layers, respectively. Due to the mechanical sliding of the motional metasurface, TMAM can achieve absorption (M_1) or reflection (M_2) functionality for incident X-band plane wave in -z direction for radar applications; and has anisotropic response for incident wave in +z direction enhances incident EM waves for C-band communication for the propose TMAM, respectively.

2.2. Multi-functional reconfigurable anisotropic metasurface design

Figs. 2 and 3 show 3D model and simulated result for the proposed TMAM periodic unit cell structure. TMAM comprises two sub-metasurface structures (top and bottom), which can be arbitrarily moved or along the x or y-axes. However, in this work, we only consider the top metasurface as a motional metasurface that is moving along the x-axis, while the bottom metasurface remains as a stationary metasurface.

Fig. 2(a) and 3(a) show different mode of M_1 and M_2 of TMAM, where the position differences of the motional metasurface are assumed to be (x, y) = [(0, 0), (Δx, 0)], where Δx = half-unit cell dimension. We achieve the repositioning of the motional metasurface by using two pair oriented SMA springs attached to different edges of the motional metasurface along x-axis. The position could be changed and controllable by activating the heat source on one of the SMA spring, where the other SMA spring remains automatically expended due to no heat source given.

The motional metasurface comprises two split-ring resonators set diagonally opposite, with lumped resistors (R_s) mounted across the gaps on the top layer. We selected R_s to maximize metasurface absorptivity, whereas the stational metasurface comprises just the two square ring resonators. We optimized each square ring resonator dimension with the consideration of the lumped resistor and has resonance at 10.5 GHz and is intended to reflect the incident wave and enhance the absorptivity of the pattern on motional metasurface.

Fig. 2(a) shows how the design creates mode M_1 when the motional metasurface is at the origin position of (x, y) = (0, 0), where the square ring resonators on the motional and stationary metasurfaces are aligned along the z-axis. We used numerical simulations to examine EM functionality for the proposed structure. Fig. 2(b) shows optimized lumped resistors for maximum M_1 occurs when R_s = 46 Ω, with the consideration of the incident wave excitation from motional metasurface side travelling in −z direction, and from stational metasurface side in +z direction. Simulated metasurface responses at 10.5 GHz operating frequency derived reflection and transmission coefficients $|\Gamma_{-z}|$ = −17.49 and $|\tau_{-z}|$ = −13.68 dB, respectively. Hence the metasurface behaves as an absorber for −z incident wave direction in M_1 mode, and as a reflec-
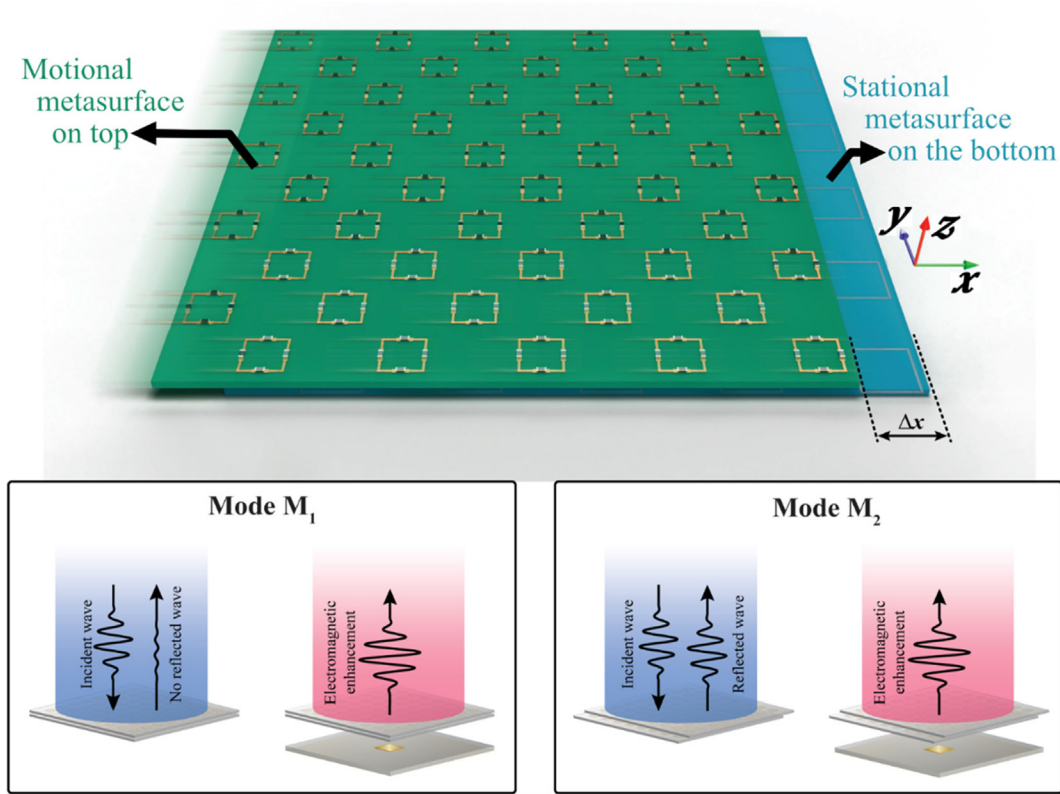
Fig. 1. Illustration of the proposed multi-functional thermal–mechanical anisotropic metasurface (TMAM).
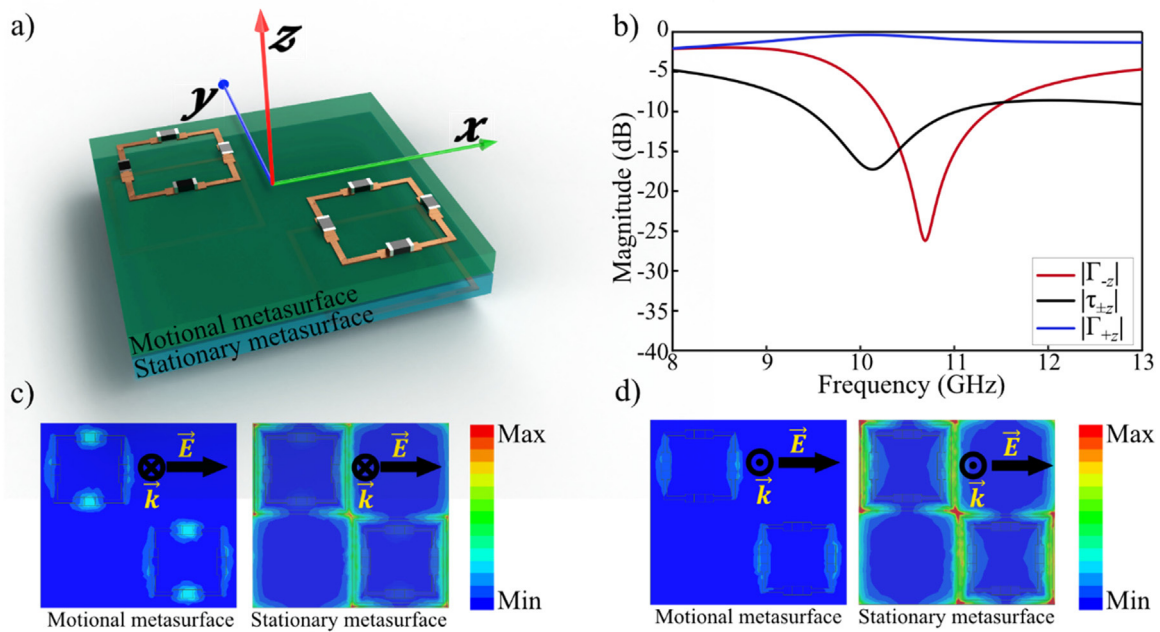

Fig. 2. M$_1$ mode unit cell design and simulation: (a) unit cell illustration where the motional metasurface is not slided, (b) simulated reflection coefficients for -z direction incident wave |Γ$_{-z}$|, +z direction incident wave |Γ$_{+z}$|, and transmission coefficient |τ$_{\pm z}$|, (c) electric field distributions on the motional and stationary metasurfaces for -z propagation direction at 10.5 GHz, (d) electric field distributions on the motional and stationary metasurfaces for +z propagation direction at 10.5 GHz.

tor with |Γ$_{+z}$| = –0.55 and |τ$_{+z}$| = –13.68 dB for +z direction incident wave, i.e., the metasurface generates absorption functionality for –z direction and reflection +z direction waves.

Fig. 2(c) and (d) shows the electrical field distribution for the top and bottom metasurface layer unit cells in M$_1$ mode. Strong

electric field occurs on the square ring resonator of the stational metasurface confirming the resonance reflector at 10.5 GHz for both-direction of the incident waves. For wave front radiation in +z incident wave direction, the motional metasurface is placed in front of the stational metasurface, the electric field existence on
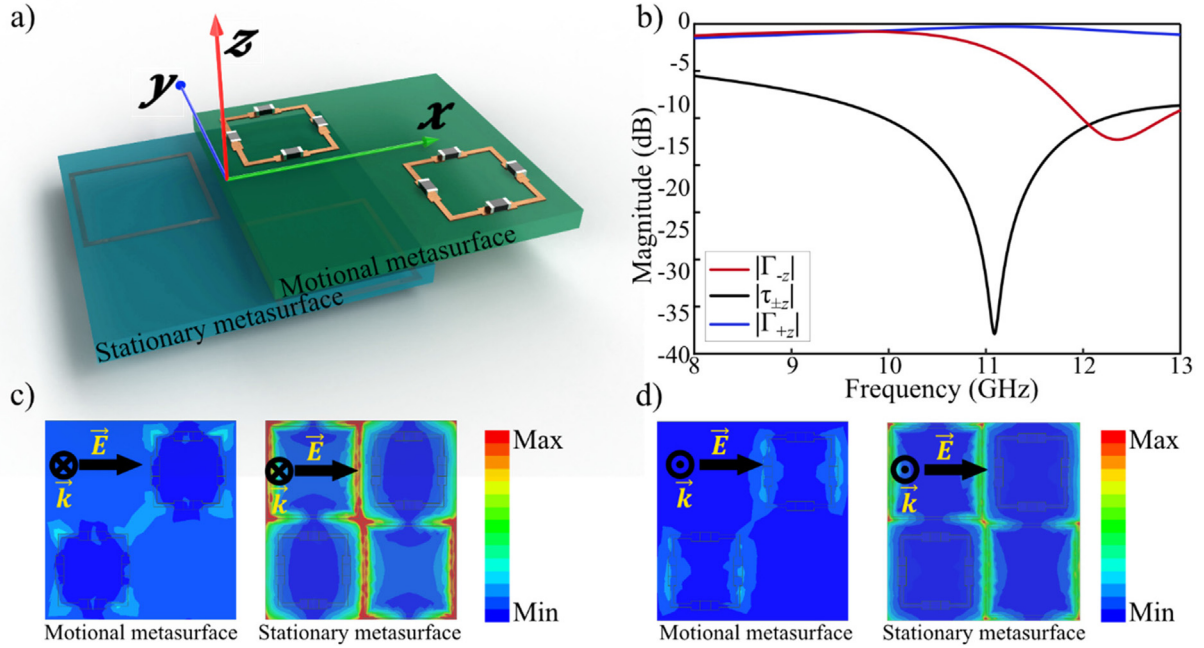
Fig. 3. M_2 mode unit cell design and simulation: (a) unit cell illustration where the motional metasurface is slided, (b) simulated reflection coefficients for -z direction incident wave $|\Gamma_{-z}|$, +z direction incident wave $|\Gamma_{+z}|$, and transmission coefficient $|\tau_{\pm z}|$, (c) electric field on the motional and stationary metasurfaces for -z propagation direction at 10.5 GHz, (d) electric field distributions on the motional and stationary metasurfaces for +z propagation direction at 10.5 GHz.

the lumped resistors showing the resonance absorption by the coupling between square ring of the motional and stational metasurface as show in Fig. 2(c). In the other hand, the motional metasurface remained at the place behind the stational metasurface for -z incident wave direction. As shown in Fig. 2(d), the coupling effect does not create the absorptivity due to the different respond of the square ring resonator in different direction of the electromagnetic wave. Hence, there is no electric field occurs at the lumped resistor.

In contrast, Fig. 3(a) shows mode M_2 occurs when the motional metasurface reaches $(x, y) = (\Delta x, 0)$, where Δx is equal to half-unit cell distance. In this case, the motional and stationary square ring resonators are completely out of alignment, which generates different input impedance compared with mode M_1. Fig. 3(b) shows the electric field distribution for mode M_2 at 10.5 GHz operation frequency, generating $|\Gamma_{-z}| = -1.452$ and $|\tau_{-z}| = -15.99$ dB for $-z$ propagation direction of incident wave, and $|\Gamma_{+z}| = -0.53$ and $|\tau_{+z}| = -15.99$ dB for $+z$ propagation direction of incident wave (Fig. S1 and Fig. S2 showing simulation setup and result of TMAM in finite structure). Fig. 3(c) and (d) shows the electrical field distribution for the motional and stational metasurface layer unit cells in M_2 mode for both propagation direction of the incident wave. In different to mode M_1, there is no electric field occurs at the lumped resistor for both direction of the incident wave, confirming the change of the input impedance of the compose square ring resonator of the motional and stational metasurface. Furthermore, the lumped resistor pattern soldering position for both motional metasurface at $(\Delta x,0)$ and $(0,0)$ allow the proposed metasurface to achieve polarization-insensitive characteristics for both M_1 and M_2 modes (Fig. S3 show reflection and absorption in different distance of motional metasurface), especially in large structure fabrication.

As discussed in Section 2.1, anisotropic response from the proposed metasurface can enhance the transmitted EM wave in the opposite (+z) direction. An integrated function for transmission wave enhancement was designed following the partially reflective

surface (PRS) in C-band communication. Distance d between the transmission antenna and proposed metasurface identifies possible enhancement for the proposed metasurface. Fig. 4 shows design properties for PRS for TMAM and subsequent transmission enhancement in simulation. Differences between metasurface modes M_1 and M_2 create differing reflection coefficients. Fig. 4(a) shows simulated reflection coefficients for -z incident wave in M_1 and M_2 modes. Reflection coefficient magnitude and phase for port 2 at 6 GHz operational frequency $|\Gamma| = 0.66$ and $\varphi = -0.83\,\pi$ (M_1) and $|\Gamma| = 0.72$ and $\varphi = -0.78\,\pi$ (M_2). The proper distance d and gain $|T|$ can be derived from [46],

$$\varphi - \pi = \frac{4\pi d}{\lambda} - 2\pi N \qquad (1)$$

and.

$$|T| = \frac{1 - \Gamma^2}{1 + \Gamma^2 - 2\Gamma\cos(\varphi - \pi - \frac{4\pi d}{\lambda})} \qquad (2)$$

where $N = 0, \pm 1, \pm 2, \ldots$; φ is the reflected phase; and λ is the wavelength. The minimum positive distance d is obtained for $N = 1$. However, the theoretical basis for Eq. (1) does not consider mutual coupling between the source metallic ground plane and the metasurface. Selecting $N = 1$ would not achieve maximum efficiency due to strong coupling with small $d < \lambda/4$. Therefore, $N = 2$ at 6 GHz would be a better selection for this analysis, and hence $d = 27.07$ and 27.67 mm for mode M_1 and M_2, respectively. In addition, the enhancement gain is calculated from Eq. (2) and show the result of $|T| = 13.77$ dB and 15.76 dB for mode M_1 and M_2."

Fig. 4(b) and (c) show simulated transmission enhancement of the proposed anisotropic metasurface. The microstrip patch antenna is used to excite EM wave toward +z direction. The enhancement ratio is defined as the ratio of the directivity with the TMAM to the directivity without the TMAM. As shown in Fig. 4(b), the simulated transmission enhancement ratio where
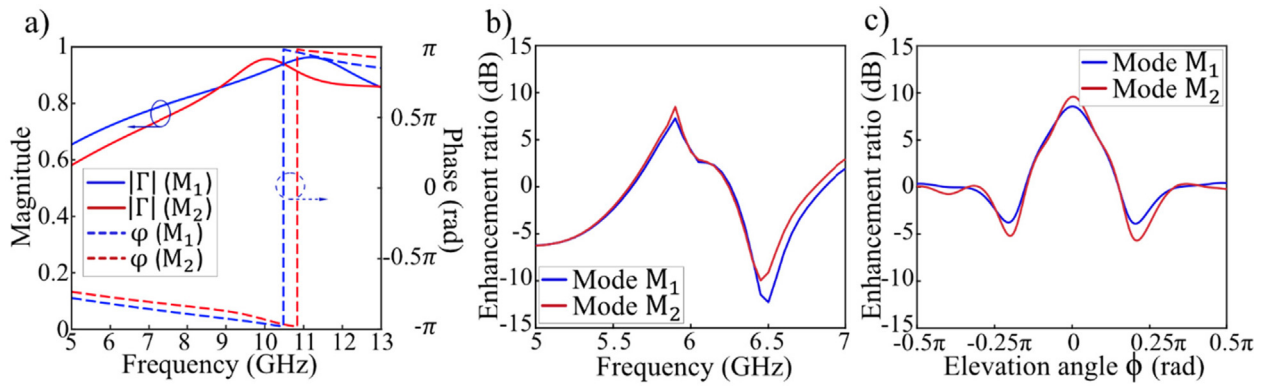
Fig. 4. Simulation results for transmission enhancement: (a) reflection coefficient magnitude |Γ| and phase φ in response to +z propagation direction, (b) transmission enhancement ratio with respect to a frequency at φ = 0, (c) the highest transmission enhancement ratio at 5.9 GHz with respect to elevation angle (φ).
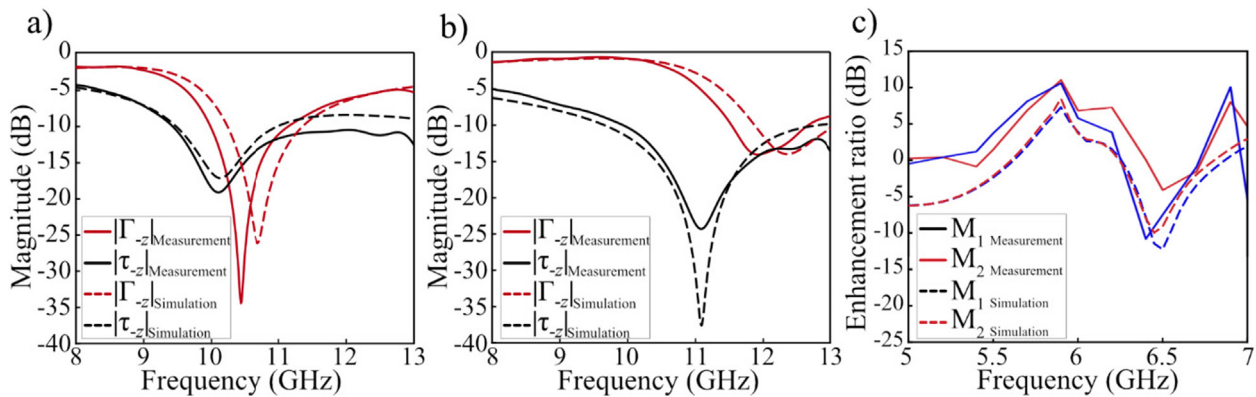

Fig. 5. Measurement and simulation results of the fabricated TMAM: (a) reflection and transmission coefficients for mode M_1, (b) reflection and transmission coefficients for mode M_2, (c) transmission enhancement ratio with respect to a frequency at φ = 0 rad for +z propagation direction.

higher than 0 dB enhancement ratio is observed from 5.45 GHz to 6.32 GHz. The maximum enhancement ratio for M_1 is 8.58 dB at 5.9 GHz while the maximum enhancement ratio for M_2 is 9.45 dB at 5.9 GHz. Fig. 4(c) shows the transmission enhancement ratio at 5.9 GHz with respect to φ. The highest enhancement is observed at φ = 0 rad.

3. Experimental verification

3.1. TMAM measurement result

We fabricated a prototype metasurface comprising 15 × 15 unit cell to validate the proposed multi-functional anisotropic metasurface performance. The motional and stational metasurface are demonstrated using common flame retardant FR-4 material, which is grade designation for glass-reinforced epoxy laminate material, with permittivity ε_r = 3.75, and tangential loss δ = 0.02 in thickness of 0.8 mm and 1 mm by printed circuit board (PCB) fabrication process. To complete the fabrication, we solder the 46 Ω chip resistor (RM04FTN46R4) on the motional metasurface using surface mount technology (SMT). In addition, we fabricated a 3D printing frame to support the sample of TMAM and SMA spring for measurement compatibility (Fig. S4).

To validate the performance of the fabricated metasurface for -z incident direction, two horn antennas are placed near the metasurface front and back (distance = 1 m) as the transmitter and receiver (Fig. S5). The measurement results for the transmission coefficients are normalized by the transmission coefficient without a sample. The measurement results for the reflection coefficients are normalized by the reflection coefficient with the copper plate. Time gating function from the vector network analyzer was used to eliminate multipath propagation. Fig. 5 shows the measured S-parameters of EM wave responses through the metasurface, where the data was filtered and recorded using an Anritsu MS2038C vector network analyzer. Fig. 5(a and b) show the measured reflection and transmission coefficients of the fabricated metasurface in modes M_1 and M_2 in different propagation direction of the incident wave. The reflection and transmission coefficients in –z propagation direction was $|\Gamma_{-z}|$ = –26.74 dB, $|\tau_{-z}|$ = –14.83 dB; and $|\Gamma_{-z}|$ = – 1.795 dB and $|\tau_{-z}|$ = –14.58 dB for mode M_1 and M_2, respectively. The measured reflection and transmission coefficients were used to calculate absorptivity. The calculated absorptivity at 10.5 GHz is 96.5% for M_1, and reflectivity at 10.5 GHz is 81.33% for M_2.

To validate the transmission enhancement for +z incident direction, the microstrip patch antenna is fabricated and its ground size has the same dimensions of the metasurface. Fig. 5(c) shows the measured transmission enhancement ratio of the fabricated TMAM at φ = 0 rad where higher than 0 dB enhancement ratio is observed from 5.5 GHz to 6.2 GHz. The maximum enhancement ratio for M_1 is 10.58 dB at 5.9 GHz while the maximum enhancement ratio for M_2 is 11.02 dB at 5.9 GHz.
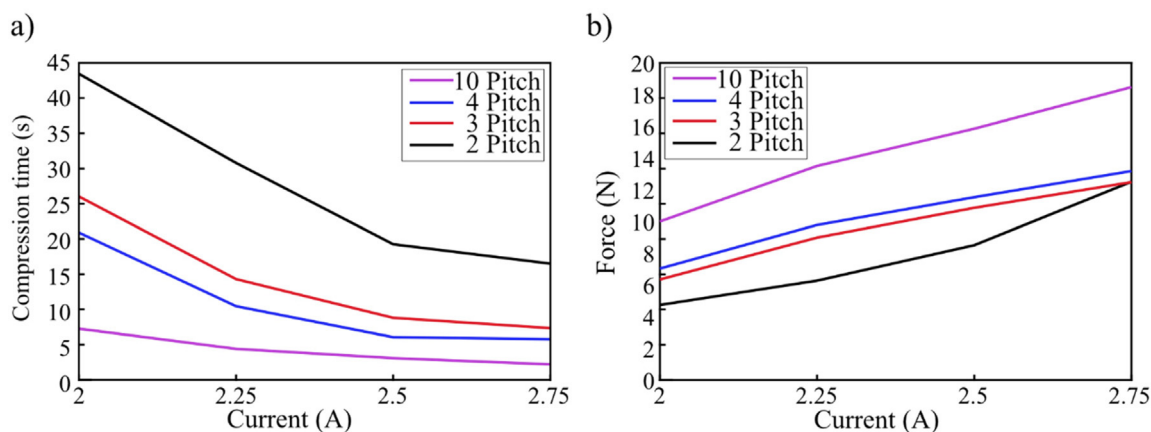
Fig. 6. Measured characteristics of the shape memory alloy spring for different pitch (length) with respect to applied current: (a) compression time, (b) compression force.

3.2. Thermal-mechanical switching conception and experiment

Shape memory alloys (SMAs) can be compressed or tensed by heating or cooling, providing a deformation mechanism to realize multi-functional metasurface switching. Heating an SMA spring above its activation temperature generates self-deformation to return to its initial form. In addition, shape memory and other self-healing material under heating and cooling thermal condition is recently being interested in study and improving [47–50]. Electrical heating is ideal to control SMA heating, and the controller can be quite small. Typical SMA springs can deform from 130 mm while requiring less than 3 A.

To support the reconfigurable of the TMAM, we use the compression type SMA spring actuator to provide the control ability of the motional metasurface movement under electrical power control panel. Fig. 6 shows typical measured SMA compression time and force with respect to applied current for various spring pitches (spring length). Fig. 6(a) shows that compression time in distance Δx is reduced for increasing current for all spring pitches: 43.4 to 16.5, 26 to 7.3, 20.9 to 5.7, and 7.2 to 2.2 s as current increased from 2 to 2.75 A, for 2, 3, 4, and 10 pitch springs, respectively. Therefore, compression time reduces for both higher current and larger pitch. Fig. 6(b) shows that spring force increases monotonically with increasing current. These data were measured at the steady state of the exponentially increasing of the force. Compression force increased 4.73 to 12.4, 6.3 to 12.4, 7 to 13.1, and 10 to 18.4 N as current increased from 2 to 2.75 A, for 2, 3, 4, and 10 pitch springs, respectively. Thus, compression force increases for both higher current and larger pitch, similar to the compression time.

4. Conclusion

This work proposed a simple and low-cost thermal–mechanical anisotropic multi-functional metasurface (TMAM) using SMA actuators thermal mechanically switching. The proposed metasurface could be reconfigured by combining two ground less sub-metasurfaces motional and stationary metasurfaces. Controlling the thermal source on two connected SMA springs to TMAM could mechanical reconfiguration between absorption and reflection for $-z$ incident plane waves; and providing anisotropic response to enhance incident EM waves travelling in the $+z$ direction. The design remains in simple and costless without using advance material, active component, and biasing layer. The incorporation of symmetric patterns for both modes, providing polarization-insensitive functionality. Measured results confirmed good agreement with simulation, validating the proposed concept. We believe the proposed TMAM concept will be suitable for many mechanical based multi-functional EM devices.

Declaration of Competing Interest

The authors declare that they have no known competing financial interests or personal relationships that could have appeared to influence the work reported in this paper.

Appendix A. Supplementary material

Supplementary data to this article can be found online at https://doi.org/10.1016/j.matdes.2022.110569.

References

[1] J.B. Pendry, D. Schurig, D.R. Smith, Controlling electromagnetic fields, Science 312 (5781) (2006) 1780–1782.
[2] J.B. Pendry, A.J. Holden, D.J. Robbins, W.J. Stewart, Magnetism from conductors and enhanced nonlinear phenomena, IEEE Trans. Microw. Theory Tech. 47 (11) (1999) 2075–2084.
[3] D.R. Smith, W.J. Padilla, D.C. Vier, S.C. Nemat-Nasser, S. Schultz, Composite medium with simultaneously negative permeability and permittivity, Phys. Rev. Lett. 84 (18) (2000) 4184–4187.
[4] D. Schurig, J.J. Mock, B.J. Justice, S.A. Cummer, J.B. Pendry, A.F. Starr, D.R. Smith, Metamaterial electromagnetic cloak at microwave frequencies, Science 314 (5801) (2006) 977–980.
[5] U. Leonhardt, Optical conformal mapping, Science 312 (5781) (2006) 1777–1780.
[6] H.-X. Xu, G.-M. Wang, K. Ma, T.J. Cui, Superscatterer illusions without using complementary media, Adv. Opt. Mater. 2 (6) (2014) 572–580.
[7] N. Kundtz, D.R. Smith, Extreme-angle broadband metamaterial lens, Nat. Mater. 9 (2) (2010) 129–132.
[8] M. Khorasaninejad, W.T. Chen, R.C. Devlin, J. Oh, A.Y. Zhu, F. Capasso, Metalenses at visible wavelengths: diffraction-limited focusing and subwavelength resolution imaging, Science 352 (2016) 1190–1194.
[9] S. Wang, Z.L. Deng, Y. Wang, Q. Zhou, X. Wang, Y. Cao, B.O. Guan, S. Xiao, X. Li, Arbitrary polarization conversion dichroism metasurfaces for all-in-one full Poincaré sphere polarizers, Light Sci. Appl. 10 (2021) 24.
[10] Z. Wu, Y. Ra'Di, A. Grbic, Tunable metasurfaces: a polarization rotator design, Phys. Rev. X. 9 (2019) 11036.
[11] H. Jeong, D.H. Le, D. Lim, R. Phon, S. Lim, Reconfigurable metasurfaces for frequency selective absorption, Adv. Opt. Mater. 8 (2020) 1902182.
[12] N.I. Landy, S. Sajuyigbe, J.J. Mock, D.R. Smith, W.J. Padilla, Perfect metamaterial absorber, Phys. Rev. Lett. 100 (2008) 207402.
[13] H.-X. Xu, G. Hu, Y. Wang, C. Wang, M. Wang, S. Wang, Y. Huang, P. Genevet, W. Huang, C.-W. Qiu, Polarization-insensitive 3D conformal-skin metasurface

cloak, Light Sci. Appl. 10 (1) (2021), https://doi.org/10.1038/s41377-021-00507-8.

[14] L. Li, T. Jun Cui, W. Ji, S. Liu, J. Ding, X. Wan, Y. Bo Li, M. Jiang, C.W. Qiu, S. Zhang, Electromagnetic reprogrammable coding-metasurface holograms, Nat. Commun. 8 (2017) 1–7.

[15] S.C. Malek, H.-S. Ee, R. Agarwal, Strain multiplexed metasurface holograms on a stretchable substrate, Nano Lett. 17 (6) (2017) 3641–3645.

[16] T.J. Cui, M.Q. Qi, X. Wan, J. Zhao, Q. Cheng, Coding metamaterials, digital metamaterials and programmable metamaterials, Light Sci. Appl. 3 (10) (2014) e218.

[17] H. Wu, S. Liu, X. Wan, L. Zhang, D. Wang, L. Li, T.J. Cui, Controlling energy radiations of electromagnetic waves via frequency coding metamaterials, Adv. Sci. 4 (2017) 1700098.

[18] N. Mohammadi Estakhri, B. Edwards, N. Engheta, Inverse-designed metastructures that solve equations, Science 363 (6433) (2019) 1333–1338.

[19] M. Camacho, B. Edwards, N. Engheta, A single inverse-designed photonic structure that performs parallel computing, Nat. Commun. 12 (2021) 1466.

[20] D.A. Pham, E. Park, H.L. Lee, S. Lim, High gain and wideband metasurfaced magnetoelectric antenna for WiGig applications, IEEE Trans. Antennas Propag. 69 (2) (2021) 1140–1145.

[21] M.R. Akram, G. Ding, K. Chen, Y. Feng, W. Zhu, Ultrathin single layer metasurfaces with ultra-wideband operation for both transmission and reflection, Adv. Mater. 32 (2020) 1907308.

[22] A.E. Cardin, S.R. Silva, S.R. Vardeny, W.J. Padilla, A. Saxena, A.J. Taylor, W.J.M. Kort-Kamp, H.T. Chen, D.A.R. Dalvit, A.K. Azad, Surface-wave-assisted nonreciprocity in spatio-temporally modulated metasurfaces, Nat. Commun. 11 (2020) 1469.

[23] S. Ghosh, S. Lim, Fluidically reconfigurable multifunctional frequency-selective surface with miniaturization characteristic, IEEE Trans. Microw. Theory Tech. 66 (8) (2018) 3857–3865.

[24] X.G. Zhang, W.X. Tang, W.X. Jiang, G.D. Bai, J. Tang, L. Bai, C.W. Qiu, T.J. Cui, Light-controllable digital coding metasurfaces, Adv. Sci. 5 (2018) 1801028.

[25] H.-X. Xu, M. Wang, G. Hu, S. Wang, Y. Wang, C. Wang, Y. Zeng, J. Li, S. Zhang, W. Huang, Adaptable invisibility management using Kirigami-inspired transformable metamaterials, Research 2021 (2021) 1–11.

[26] H.-X. Xu, S. Ma, X. Ling, X.-K. Zhang, S. Tang, T. Cai, S. Sun, Q. He, L. Zhou, Deterministic approach to achieve broadband polarization-independent diffusive scatterings based on metasurfaces, ACS Photonics 5 (5) (2018) 1691–1702.

[27] R. Phon, S. Ghosh, S. Lim, Novel multifunctional reconfigurable active frequency selective surface, IEEE Trans. Antennas Propag. 67 (3) (2019) 1709–1718.

[28] Q. Ma, G.D. Bai, H.B. Jing, C. Yang, L. Li, T.J. Cui, Smart metasurface with self-adaptively reprogrammable functions, Light Sci. Appl. 8 (2019) 98.

[29] B. Rana, L.-G. Lee, I.-P. Hong, Experimental Characterization of 2 × 2 Electronically Reconfigurable 1 Bit Unit Cells for a Beamforming Transmitarray at X Band, J Electromagn Eng Sci. 21 (2021) 153, https://doi.org/10.26866/jees.2021.21.2.153.

[30] R. Phon, S. Ghosh, S. Lim, Active frequency selective surface to switch between absorption and transmission band with additional frequency tuning capability, IEEE Trans. Antennas Propag. 67 (9) (2019) 6059–6067.

[31] Y. Guo, S. Zhang, M. Pu, Q. He, J. Jin, M. Xu, Y. Zhang, P. Gao, X. Luo, Spin-decoupled metasurface for simultaneous detection of spin and orbital angular momenta via momentum transformation, Light Sci. Appl. 10 (1) (2021), https://doi.org/10.1038/s41377-021-00497-7.

[32] Y. Zhang, H. Liu, H. Cheng, J. Tian, S. Chen, Multidimensional manipulation of wave fields based on artificial microstructures, Opto-Electron Adv. 3 (2020) 200002–200032.

[33] S. Savo, D. Shrekenhamer, W.J. Padilla, Liquid crystal metamaterial absorber spatial light modulator for THz applications, Adv. Opt. Mater. 2 (3) (2014) 275–279.

[34] K. Dong, S. Hong, Y. Deng, H. Ma, J. Li, X. Wang, J. Yeo, L. Wang, S. Lou, K.B. Tom, K. Liu, Z. You, Y. Wei, C.P. Grigoropoulos, J. Yao, J. Wu, A Lithography-free and field-programmable photonic metacanvas, Adv. Mater. 30 (2018) 1–7.

[35] J. Shabanpour, S. Beyraghi, A. Cheldavi, Ultrafast reprogrammable multifunctional vanadium-dioxide-assisted metasurface for dynamic THz wavefront engineering, Sci. Rep. 10 (2020) 1–14.

[36] S.A. Nauroze, L.S. Novelino, M.M. Tentzeris, G.H. Paulino, Correction: continuous-range tunable multilayer frequency-selective surfaces using origami and inkjet printing, Proc. Natl. Acad. Sci. U. S. A. 115 (2018) 13210–13215, doi: 10.1073/pnas.1812486115. Proc. Natl. Acad. Sci. U. S. A. 166 (2019) 11074.

[37] Z. Wang, L. Jing, K. Yao, Y. Yang, B. Zheng, C.M. Soukoulis, H. Chen, Y. Liu, Origami-based reconfigurable metamaterials for tunable chirality, Adv. Mater. 29 (2017) 1–7.

[38] Z. Liu, H. Du, J. Li, L. Lu, Z.Y. Li, N.X. Fang, Nano-kirigami with giant optical chirality, Sci. Adv. 4 (2018) 1–9.

[39] F. Zhang, X. Xie, M. Pu, Y. Guo, X. Ma, X. Li, J. Luo, Q. He, H. Yu, X. Luo, Multistate switching of photonic angular momentum coupling in phase-change metadevices, Adv. Mater. 32 (2020) 1–9.

[40] M. Li, L. Shen, L. Jing, S. Xu, B. Zheng, X. Lin, Y. Yang, Z. Wang, H. Chen, Origami metawall: mechanically controlled absorption and deflection of light, Adv. Sci. 6 (23) (2019) 1901434, https://doi.org/10.1002/advs.v6.2310.1002/advs.201901434.

[41] R. Phon, Y. Kim, E. Park, H. Jeong, S. Lim, Mechanical and self-deformable spatial modulation beam steering and splitting metasurface, Adv. Opt. Mater. 2100821 (2021) 202100821.

[42] S.I.H. Shah, A. Sarkar, R. Phon, S. Lim, Two-dimensional electromechanically transformable metasurface with beam scanning capability using four independently controllable shape memory alloy axes, Adv. Opt. Mater. 8 (2020) 202001180.

[43] L. Zhang, R.Y. Wu, G.D. Bai, H.T. Wu, Q. Ma, X.Q. Chen, T.J. Cui, Transmission-reflection-integrated multifunctional coding metasurface for full-space controls of electromagnetic waves, Adv. Funct. Mater. 28 (2018) 1–9.

[44] Y. Zhao, J. Gao, X. Cao, T. Liu, L. Xu, X. Liu, L. Cong, In-band RCS reduction of waveguide slot array using metasurface bars, IEEE Trans. Antennas Propag. 65 (2) (2017) 943–947.

[45] L.Y. Ji, Y.J. Guo, P.Y. Qin, G. Fu, A reconfigurable beam-scanning partially reflective surface (PRS) antenna, in: 2015 9th Eur. Conf. Antennas Propagation, EuCAP 2015. 63 (2015) 2387–2395.

[46] G.V. Trentini, Partially reflecting sheet arrays, IRE Trans. Antennas Propag. 4 (4) (1956) 666–671.

[47] W. Gao, X. Yi, G. Song, Z. Wang, X. Meng, Zr50Cu25Ni7.5Co17.5 high-temperature shape memory alloy with excellent thermal stability and large recovery strain, and the associated microstructural deformation mechanism, Mater. Des. 196 (2020) 109108.

[48] M. Zelený, P. Sedlák, O. Heczko, H. Seiner, P. Veřtát, M. Obata, T. Kotani, T. Oda, L. Straka, Effect of electron localization in theoretical design of Ni-Mn-Ga based magnetic shape memory alloys, Mater. Des. 209 (2021) 109917, https://doi.org/10.1016/j.matdes.2021.109917.

[49] C. You, Y. Kang, M.S. Kim, Y. Ahn, H. Kye, B.-G. Kim, Octagonal-siloxane based transparent and robust crack-healing surface for optical-scar recovery, Mater. Des. 215 (2022) 110475.

[50] J. Zhao, M. Han, L. Li, Modeling and characterization of shape memory properties and decays for 4D printed parts using stereolithography, Mater. Des. 203 (2021) 109617.